Soft Matter

PAPER

View Article Online
View Journal | View Issue

Cite this: *Soft Matter*, 2016, 12, 1759

Multiscale flow in an electro-hydrodynamically driven oil-in-oil emulsion†

Atul Varshney,*[ab] Smita Gohil,[b] Mayur Sathe,[c] Seshagiri Rao R V,[d] J. B. Joshi,[e] S. Bhattacharya,[b] Anand Yethiraj*[df] and Shankar Ghosh*[b]

Received 14th September 2015,
Accepted 9th December 2015

DOI: 10.1039/c5sm02316e

www.rsc.org/softmatter

Efficient mixing strategies in a fluid involve generation of multi-scale flows which are strongly suppressed in highly viscous systems. In this work, we report a novel form of multi-scale flow, driven by an external electric field, in a highly viscous ($\eta \sim 1$ Pa s) oil-in-oil emulsion system consisting of micron-size droplets. This electro-hydrodynamic flow leads to dynamical organization at spatial scales much larger than that of the individual droplets. We characterize the dynamics associated with these structures by measuring the time variation of the bulk Reynolds stress in a rheometer, as well as through a micro-scale rheometric measurement by probing the spectrum of fluctuations of a thin fiber cantilever driven by these flows. The results display scale invariance in the energy spectra over three decades with a power law reminiscent of turbulent convection. We also demonstrate the mixing efficiency in such micro-scale systems.

Introduction

Multi-scale fluid flow occurs in many natural phenomena. One example is in fluid turbulence, which is represented as an energy-cascade flowing from larger scale eddies to smaller ones where it is dissipated due to viscosity.[1] In pipe-flow of Newtonian fluids driven by pressure gradients the flow becomes unsteady when nonlinear inertial forces exceed the dissipative viscous forces, around the Reynolds number Re $\sim$ 2000, where Re is the ratio of inertial-to-viscous forces.[2,3] Multi-scale flows have also been observed at very low Re in non-Newtonian fluids, *e.g.* elastic turbulence in polymer solutions[4] and meso-scale turbulence in dense suspensions of "active" self-driven systems.[5,6] The source of the non-linearity in polymer solutions has been attributed to the presence of elastic stresses that arise from the conformational change of polymer molecules during the flow, whereas in active systems the non-linearity arises from mutual interactions. Gaining control over the multi-scale flow is also of practical importance. Such control can be achieved in micro-scale self-organizing systems, where one is able to control microscopic interactions through which the connection between interactions at smaller scale and the resulting large scale flow can be elucidated.[7]

There are many applications where the accelerated rate of mass transport afforded by multi-scale fluid flow is desirable. One such situation of great industrial importance is mixing.[8] Situations involving mixing where the Reynolds number is small, such as in microfluidic devices, require vigorous shear-induced mixing.[9] This is an inefficient process because viscous dissipation suppresses the occurrence of multi-scale flow in low Reynolds number systems. Chaotic mixing has been achieved by elegant means,[10] but in a flow-through geometry.

In this work, we present a new system – a micron-scale oil-in-oil emulsion – where mixing is achieved, in a non-flow-through geometry and in the presence of sub-millimeter scale confinement, *via* control of electrohydrodynamic flows across multiple time and length scales. The multi-scale flow observed here straddles the paradigms of scale-invariant turbulent systems and self-organizing active matter systems. We demonstrate an unprecedented level of control, both of the strength of the hydrodynamic interactions with an external electric field, and of the energy-injection length scale *via* the size of the droplets. We then obtain multiple measures of these unsteady flows using macro- and micro-scale rheometry, as well as through concurrent optical microscopy and find self-consistent power law scaling in the energy spectrum. We also demonstrate the mixing efficiency in such micro-scale systems through the dispersion of dye.

[a] *Department of Physics of Complex Systems, Weizmann Institute of Science, Rehovot 76100, Israel. E-mail: atul.varshney@weizmann.ac.il*
[b] *Department of Condensed Matter Physics and Materials Science, Tata Institute of Fundamental Research, Homi Bhabha Road, Mumbai 400 005, India. E-mail: sghosh@tifr.res.in*
[c] *Cain Department of Chemical Engineering, Louisiana State University, LA 70803, USA*
[d] *TIFR Centre for Interdisciplinary Sciences, Osman Sagar Road, Narsingi, Hyderabad 500 075, India*
[e] *Homi Bhabha National Institute, Anushaktinagar, Mumbai 400 094, India*
[f] *Department of Physics and Physical Oceanography, Memorial University, St. John's, Newfoundland Labrador, Canada A1B 3X7. E-mail: ayethiraj@mun.ca*

† Electronic supplementary information (ESI) available. See DOI: 10.1039/c5sm02316e

In the presence of an electric field, the difference in the conductivity of a liquid drop and its surrounding liquid results in the formation of surface charges on the drop. The characteristic charge relaxation time (τ_c) in the drop phase and in the surrounding liquid phase is given by the ratio of the permittivity (ε) and conductivity (σ) of the respective medium. When τ_c is larger for the drop phase than for the medium, the drop undergoes spontaneous rotation[11] in the presence of field: for an isolated drop, the axis of rotation lies in the plane normal to the electric field vector. In addition, the combination of an electric field and a charged interface gives rise to electrohydrodynamic forces, which cause circulatory flows inside and outside the drop, leading to drop deformation. This scenario is well captured in the leaky dielectric model presented by Melcher and Taylor[12] and studied extensively thereafter.[13,14]

Hydrodynamic interactions are long ranged, and the velocity associated with the rotational flow generated by a droplet decays inversely with the square of the distance.[15] Neighboring droplets respond to the electric-field-induced fluid flow in multiple ways: moving,[16] deforming, breaking up, or coalescing – a detailed study of the frequency-dependent phase diagram was reported earlier[17] and dc fields were found to provide the strongest hydrodynamic interactions. Beyond a critical value of the field, an "active" regime appears where a convective electrokinetic instability sets in that generates spatial variations in droplet concentration in the system and an emergent collective flow pattern is observed. Such instabilities have been observed in nematic liquid crystals[18] and in electrolytes.[19,20]

Experimental

Our system consists of an oil-in-oil emulsion, prepared by mixing silicone oil (a dielectric) and castor oil (a leaky dielectric) in a volume ratio of 1 : 3 in a vortex shaker. The castor oil forms the continuous phase while the dispersed droplets are of silicone oil (see Fig. 1(a)). The high viscosity of the liquids ensures, even in the absence of a surfactant, that the quiescent emulsion is stable for days. In the absence of an external field, the oil-in-oil mixture is Newtonian, exhibiting a clean, linear dependence of stress on shear rate (see Fig. S1, ESI†). The material constants for silicone and castor oils are tabulated in Table S1 (ESI†). The experimental set-up is shown schematically in Fig. 1(b). The emulsion was placed between two ITO coated electrodes (spaced 300 μm apart), mounted in the parallel plate geometry onto a rheometer (Anton Paar; MCR301), and imaged from below using a high-speed camera (PCO 1200s) with a 4× magnification objective (NA = 0.2, working distance = 15.7 mm). The illumination is provided from the top by a customized LED light source. An alternate (microrheometric) setup involved an optical fiber cantilever that was clamped at the edge of the cell but tapered to a diameter of 30 μm inside the cell which allows optical measurements, with a 10× magnification objective and a CMOS camera (PCO; Edge 4.2), of cantilever fluctuations driven by the hydrodynamic flows. An external dc electric field is applied across the electrodes by using a high voltage source (SRS PS375).

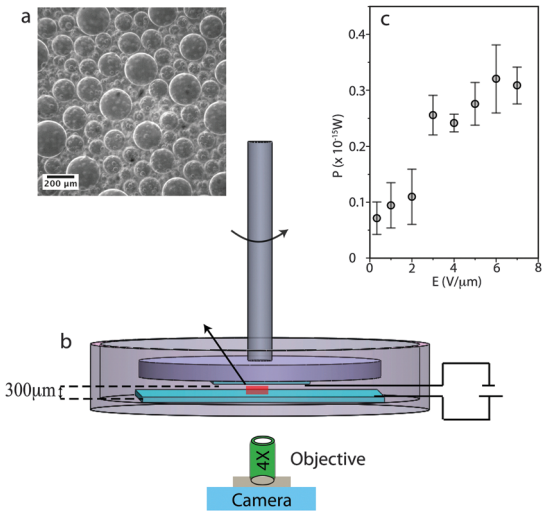

Fig. 1 (a) The micrograph shown is a snapshot of the emulsion at zero field. The silicone oil droplets are dispersed in the continuous phase of castor oil. (b) A rheometer, shown schematically, is used to measure shear stress in an oil–oil emulsion system. The red rectangular box shows the region that is being imaged between the electrodes. It is also the region where a thin optical fiber is placed as a cantilever that responds to the hydrodynamic flows. (c) Electrical power drawn (P) as a function of E.

Results and discussion

Droplet imaging and velocimetry

Upon increasing the electric field from E = 0 to 6.7 V μm^{-1}, we observe a violent breakup of large drops into smaller droplets (Movie 1, ESI†), coupled with unsteady flows. The observation of drop breakup is consistent with an increase in the electrical power drawn by the system above E = 3 V μm^{-1} (see Fig. 1(c)), and is accompanied by enhanced drop motion. The strength of the motion increases dramatically with increasing field, and the system enters the active regime where drop sizes are independent of the initial conditions. The droplets continually split into daughter structures and recombine: while the interfacial electrostatic stresses aid their break-up, surface tension provides the stabilizing force opposing the production of smaller sized drops. At each electric field, we observe a steady-state distribution of droplet sizes $N(a)$, which is shown as a function of the drop radius a for $E > 6$ V μm^{-1} in Fig. 2. For fields larger than E = 6.7 V μm^{-1} there is a steady state droplet size distribution, and a log-normal form (as indicated in ref. 21) can be fit to the size distributions, yielding a mean droplet radius = 22 ± 1.3 μm. The key point is that there is a lengthscale (the Hinze scale a_H; highlighted with gray bands in Fig. 2) above which drops do not survive. The existence of a typical lengthscale for bubbles in turbulent shear flow was recognized by Hinze,[22] who obtained a_H by equating the disrupting differential pressure forces (σ_D) on the droplets' surface to the restoring forces due to surface tension (γ), defined as $a_H \sim \gamma/\sigma_D$. The inset of Fig. 2 shows the variation of a_H with E (computed, as elsewhere,[23] by thresholding the cumulative count of $N(a)$ at 95%). In the present experiments the differential pressure forces arise due to both the induced flow and the accumulated surface charges. The effect of the shear flow

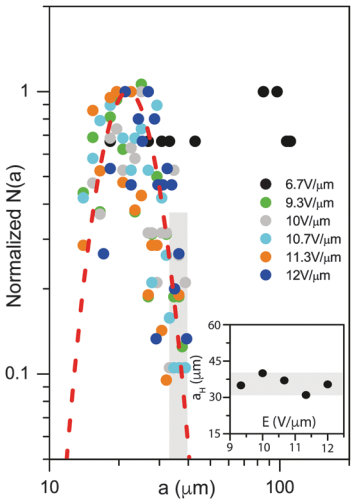

Fig. 2 The variation of droplet size distribution $N(a)$ normalized with its maximum value with drop radius a for fields above 6 V μm^{-1} is lognormal (red dashed line) with the form $s(a) = e^{-(\log_e(a)-\mu)^2/(2\Sigma^2)}/a\sqrt{2\pi\Sigma^2}$. The fit yields mean droplet radius = 22 ± 1.3 μm, for $E > 9$ V μm^{-1}. The gray bands represent the range of values calculated for a_H.

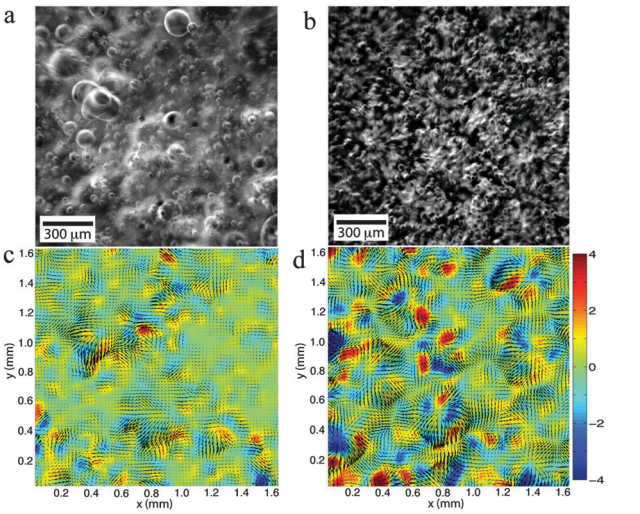

Fig. 3 Snapshots of the system at (a) E = 6.7 V μm^{-1} and (b) 12 V μm^{-1}. Typical velocity (shown by arrows) and vorticity (the color map in units of s^{-1}) fields obtained from particle image velocimetry (PIV) for (c) E = 6.7 V μm^{-1} and (d) 12 V μm^{-1}, with v_{rms} = 20 and 100 μm s^{-1} respectively.

is reflected in the deformations of the droplets (see Fig. S2, ESI†) while the effect of buildup of surface charges is evident for droplets of larger size which burst into smaller ones.

The dynamics of the system was simultaneously captured by three techniques: (i) macro-scale rheology using a conventional rheometer, (ii) micro-scale rheology *via* the imaging of micro-scale cantilever fluctuations, and (iii) direct optical imaging of droplet motions which we discuss first. Fig. 3(a) and (b) show representative optical micrographs of the droplet motions at electric fields E = 6.7 and 12 V μm^{-1} respectively. For $E < 6.7$ V μm^{-1}, only a periodic convective motion exists in the system, accompanied by droplet breakup and coalescence events. For increasing values of E, however, the flow patterns become random; they initially generate an isotropic chaotic motion of the droplets without producing any distinctive spatial structures (E = 6.7 V μm^{-1}) (see Fig. 3(a) and Movie 1, ESI†). For $E > 10$ V μm^{-1}, flow generated coherent structures are observed (see Fig. 3(b) and Movie 2, ESI†). Here, the droplets are not uniformly dispersed; instead they form dynamic clusters that are reasonably dense (area fractions of ∼0.45) which are spatially separated regions of high vorticity (see Fig. 3(d)). With increasing field, these clusters become more space filling, though their internal structure does not evolve appreciably (see Fig. S3, ESI†).

The corresponding spatial velocity and vorticity maps, shown in Fig. 3(c) and (d) respectively, are obtained from particle image velocimetry (PIV) extracted from the motion of droplets (see Fig. S4, ESI†). We also use the spatial-temporal information from the PIV in Fig. 3(c) and (d) to obtain power spectrum as a function of the spatial frequency k, and a power law scaling, albeit over just one decade, with an exponent α_k = 1.39 ± 0.02 is observed (see Fig. 4). The variation of mean and root mean square velocities with E is shown in Fig. S5 (ESI†).

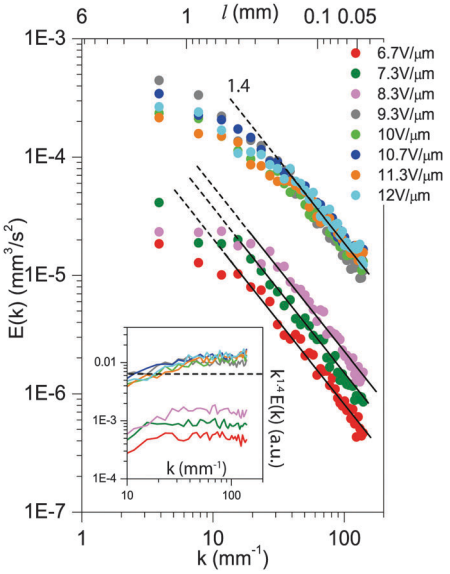

Fig. 4 The power spectrum, $E(k)$ *vs.* k, of turbulent droplet motion in the active regime at different field values. It is fitted to a $k^{-\alpha_k}$ dependency which yields α_k = 1.39 ± 0.02 as shown by the solid line (the dashed line indicates the deviation from power law behavior at small k). The inset shows the consolidated plots, *i.e.*, $k^{1.4}E(k)$, for different E.

Macro-scale rheometry

Macroscopic rheological measurements reveal time evolution of the electric field induced shear stresses, measured at the top electrode. Fig. 5(a) shows the time series of shear stress fluctuations ($\tau - \langle\tau\rangle$), where $\langle\cdots\rangle$ denotes the time average, for various values (each with a different color) of E. We identify it as the Reynolds shear stress, *i.e.*, the contribution of turbulent motion to the mean shear stress.[1] The data clearly demonstrate that the internal flow in the cell, which produces fluctuating stress at the walls, becomes increasingly unsteady

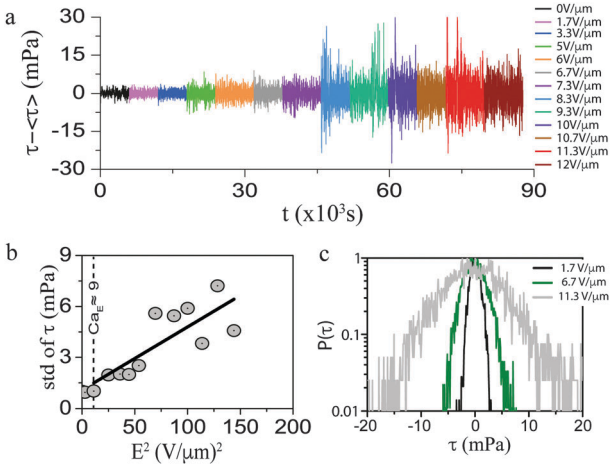

Fig. 5 (a) Temporal fluctuations of shear stress, $\tau - \langle\tau\rangle$, with increasing electric field E. (b) The standard deviation of shear stress fluctuations (shown in (a)) plotted against E^2 exhibits a linear increase above a critical value of $E \sim 3$ V μm^{-1}, which corresponds to $Ca_E \approx 9$. (c) The normalized probability distribution of $(\tau - \langle\tau\rangle)$, $P(\tau)$, broadens with increasing E.

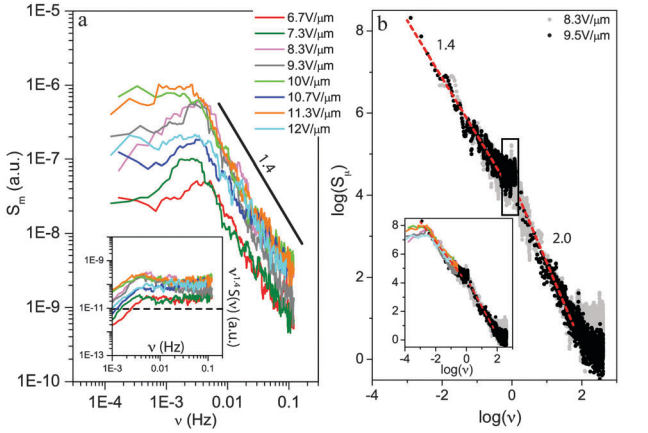

Fig. 6 (a) Power spectrum, $S_m(\nu)$, of macroscopic shear stress fluctuations obtained from rheometry at different fields E. The power of fluctuations increases but the frequency dependence of the spectra remains the same and follows a $\nu^{-\alpha_\nu}$ power law dependence for over a decade of frequencies. A global fit for all electric fields to one value of α_ν yields $\alpha_\nu = 1.38 \pm 0.02$. The inset shows the consolidated plots, *i.e.*, $\nu^{1.4}S(\nu)$, for different electric field values. (b) The power spectrum of micro-scale fluctuations $S_\mu(\nu)$ of an optical fiber cantilever, shown on a log–log plot, enables access to higher frequencies. A regime of power-law scaling with $\alpha_\nu = 1.4$ is also seen in these microscale measurements up to 1 Hz, where we see droplet convection. The inset shows collapse of all power spectra in (a) and (b) in the regime $-3 < \log(\nu) < 0$.

with increasing E. In Fig. 5(b), we observe that the standard deviation of the Reynolds stress, $(\tau - \langle\tau\rangle)$, a measure of the strength of the unsteady flow, grows linearly as a function of the electric field intensity E^2 above an electric field value of ~ 3 V μm^{-1}. This is also concurrent with the field strength at which the system shows a sudden increase in the electrical power intake (see Fig. 1(c)). The relative strength of the electrostatic and surface tension forces is given by the electric capillary number $Ca_E = \varepsilon_0\varepsilon_s E^2 a/\gamma$, where ε_0 is the free space permittivity and ε_s is the dielectric constant of the droplet of size a; $Ca_E > 1$ would suggest the deformation of the droplet from its spherical shape. In our experiments, the onset of unsteady flow appears at $E > 3$ V μm^{-1} (see Fig. 1(c) and 5(b)) which corresponds to $Ca_E \approx 9$ for $a \sim 100$ μm. The corresponding normalized probability distribution of $(\tau - \langle\tau\rangle)$, $P(\tau)$, shown in Fig. 5(c) for E = 1.7, 6.7 and 11.3 V μm^{-1}, closely resembles Gaussian distributions. The time series of stress fluctuations is averaged over the entire surface of the detector and hence is only sensitive to slowly varying fluctuations happening over a large scale.

Fig. 6(a) shows the power spectrum, $S_m(\nu)$, of the time series data of the Reynold shear stress $(\tau - \langle\tau\rangle)$ for different values of E. Strikingly, all the graphs have similar features: there is a peak in $S(\nu)$ at around 2–3 mHz, and from $\nu_{low} = 3$ mHz to $\nu_{high} = 0.1$ Hz, the power spectrum exhibits a $S(\nu) \sim \nu^{-\alpha_\nu}$ power law. Results at all the fields shown are fit globally to a single value of α_ν: this yields $\alpha_\nu = 1.38 \pm 0.02$. Assuming a linear dispersion relation $2\pi\nu \sim v_{rms}k$, where v_{rms} is the root-mean-square velocity and k is the wave-vector, the frequencies ν_{low} and ν_{high} are related to lengthscales $\ell = 2\pi/k = v_{rms}/\nu$ which are 50 mm and 1 mm respectively, using $v_{rms} = 100$ μm s^{-1}; these lengthscales are thus larger than the cell spacing of 300 μm but comparable to the lateral extent (50 mm) of the system (see Fig. 4).

Micro-scale rheometry

In a separate experiment, we examine the spectrum of fluctuations of a fiber cantilever immersed in the flow. Experiments at two different field values in the active regime (E = 8.3 and 9.5 V μm^{-1}) and two acquisition rates (812.9 and 9.97 frames per second) are shown in a single plot in Fig. 6(b). Since the fiber diameter is ~30 μm, it measures flow induced stresses at the droplet lengthscale. In Fig. 6(b), we plot the power spectrum, $S_\mu(\nu)$, of these fluctuations *versus* the temporal frequency ν, on a logarithmic scale. It should be noted that, in the overdamped regime, the fluctuations in cantilever position are proportional to stress fluctuations. Here we are able to span about 5 decades in frequency. Below 1 Hz ($\log(\nu) = 0$), we find that there is a power law $S_\mu(\nu) \sim \nu^{-\alpha_\nu}$ scaling with a fitted value of $\alpha_\nu = 1.40 \pm 0.04$. At a characteristic frequency $\nu_c \sim 1$ to 3 Hz (depending on amplitude), there exists a minor peak. Above ν_c (for $0 < \log(\nu) < 2$), there is a different scaling with a power law $\alpha_\nu = 2.0 \pm 0.03$. The power law exponent of −2 likely arises from the spectral response of the cantilever at high frequencies while the peak at about 1 Hz is associated with the frequency of visible convective motion of droplets. This convective motion can be seen in Movie 3 (ESI†), corresponding to an acquisition of a small area near the cantilever, at 116 fps, where droplets can be seen going in and out of focus with a period of approximately 0.5 second. The big drop rotates, while the small ones revolve around the big one: both are driven by the underlying fluid flow.

In conventional turbulence the length scale at which the energy is injected to the system is well defined.[1] This energy is then progressively distributed towards smaller scales, described through the relevant power-spectrum. The present experiments suggest an alternative scenario: the electrical energy is directly injected to the droplets which generates their motion. As the field increases, the activity of these droplets increases. At high fields,

corresponding to $Ca_E \gg 1$, drops deform and break. In addition drops move, coalesce and form clusters. All of this yields a broad distribution of droplet sizes and the system self-organizes to form cellular structures of convective flows. Thus, the steady state reflects a multiplicity of energy injection length scales.

Mixing

To demonstrate the mixing efficiency of the system, the following experiment is performed. The prepared emulsion (see Experimental section) is divided into two portions. The first portion is used to partially fill the rectangular cell (of dimension 25 mm × 4 mm × 0.25 mm). In the second portion the oil red O dye is added to give it a red color. The dyed emulsion is then used to fill the rest of the cell. It produces a clearly detectable front in the cell (see the micrograph at $t = 0$ in the top inset of Fig. 7). The height of the front (h) is measured with respect to the initial height (h_0) at $t = 0$. The system is kept in a horizontal position and on application of the field the dye begins to diffuse at a much faster rate. The top inset of Fig. 7 displays the micrographs captured at different times (marked above each image) of the dispersion for $E = 5$ V μm^{-1}. The image in the bottom inset of Fig. 7 shows the corresponding time evolution of h, which varies as square root of t, *i.e.*, $h = h_0 + \sqrt{2D_{\text{eff}}t}$, as shown by the yellow dashed line. The grayscale intensity is averaged over the cell width; the darker region corresponds to the space where the dye has spread. The variation of the effective dispersion coefficient (D_{eff}) as a function of E is plotted in Fig. 7. Clearly the mixing begins to occur for $E > 3$ V μm^{-1}, in accordance with the onset of flow in the system (see Fig. 1(c) and 5(b)). The dyed fluid is transported and spread across the length of the cell by the multi-scale flow arising from the collective motion of the droplets, thereby enhancing the mixing of viscous fluids in a micro-scale system (see Movie 4, ESI†). The typical value of the molecular diffusivity (D) of the oil used[24] is $\sim 10^{-6}$ mm^2 s^{-1}; thus the ratio $D_{\text{eff}}/D \sim \mathcal{O}(10^4)$. The largeness of the ratio suggests that turbulent dispersion is the dominant mechanism for the mixing.

The experiments with dye also shed some light on the self-organization process. The system organizes into cellular clusters, whose length scale is comparable to the cell thickness. With increasing field, this length scale remains unchanged (see Fig. S3, ESI†).

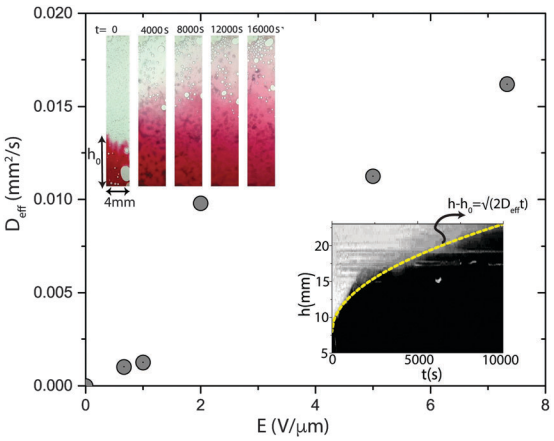

Fig. 7 Variation of effective dispersion coefficient (D_{eff}) with E. The top inset displays micrographs captured at different times (marked above each image) for $E = 5$ V μm^{-1}. At $t = 0$, the height of the dyed front (in red color) is h_0. The grayscale image in the bottom inset shows the time evolution of h, which varies as $h - h_0 = \sqrt{2D_{\text{eff}}t}$, highlighted by the yellow dashed line. The dark region in the grayscale map corresponds to the space occupied by the dye, and *vice versa*.

Conclusions

We have characterized the multi-scale flow that arises on application of an electric field in an oil-in-oil emulsion system. Three independent experimental modalities were employed to obtain the power spectra in both space and time: they are all consistent with the power law scalings that exemplify multi-scale spatio-temporal flow.

Beyond a critical value of the field, a convective electrokinetic instability sets in that generates spatial variations in the droplet concentration in the system and an emergent collective flow pattern is observed. However, the mechanism of convective instability in our system is still unclear and we plan to explore its origin in a future study.

Multi-scale flow has also been observed in linear pipe flow of polymer solutions[25] with a direct energy cascade (as in conventional turbulence) from large to small scales. In our experiments, however, the source of the nonlinearity that leads to multi-scale flow comes from droplet deformation and breakup. The present experiment illustrates a unique situation where energy is injected into the continuous phase at multiple length scales, length scales that extend from a single drop to multi-drop clusters. In this self-organizing multi-scale flow, we demonstrate that turbulent dispersion is the dominant mechanism for mixing at micro-scales.

Acknowledgements

A. V. thanks Pankaj Mishra for helpful discussions. A.Y. thanks members of the TIFR (Mumbai) soft matter group as well as TCIS Hyderabad for generous hospitality during the course of these studies, as well as the Physical Oceanography group at Memorial University and Prasad Perlekar at TCIS Hyderabad for useful advice. This work was supported in part by NSERC.

References

1 H. Tennekes and J. L. Lumley, *A First Course in Turbulence*, The MIT Press, 1972.
2 O. Reynolds, *Philos. Trans. R. Soc. London*, 1883, **174**, 935–982.
3 K. Avila, D. Moxey, A. d. Lozar, M. Avila, D. Barkley and B. Hof, *Science*, 2011, **333**, 192–196.
4 A. Groisman and V. Steinberg, *Nature*, 2000, **405**, 53–55.
5 H. H. Wensink, J. Dunkel, S. Heidenreich, K. Drescher, R. E. Goldstein, H. Löwen and J. M. Yeomans, *Proc. Natl. Acad. Sci. U. S. A.*, 2012, **109**, 14308–14313.

6 J. Dunkel, S. Heidenreich, K. Drescher, H. H. Wensink, M. Bär and R. E. Goldstein, *Phys. Rev. Lett.*, 2013, **110**, 228102.
7 A. Bricard, J.-B. Caussin, N. Desreumaux, O. Dauchot and D. Bartolo, *Nature*, 2013, **503**, 95–98.
8 *Handbook of industrial mixing: science and practice*, ed. E. L. Paul, V. A. Atiemo-Obeng and S. M. Kresta, Wiley-Interscience, Hoboken, N.J, 2004.
9 M. Lopez and M. D. Graham, *Phys. Fluids*, 2008, **20**, 053304.
10 A. D. Stroock, S. K. W. Dertinger, A. Ajdari, I. Mezić, H. A. Stone and G. M. Whitesides, *Science*, 2002, **295**, 647–651.
11 T. Jones, *IEEE Trans. Ind. Appl.*, 1984, **IA–20**, 845–849.
12 J. R. Melcher and G. I. Taylor, *Annu. Rev. Fluid Mech.*, 1969, **1**, 111–146.
13 D. A. Saville, *Annu. Rev. Fluid Mech.*, 1997, **29**, 27–64.
14 P. F. Salipante and P. M. Vlahovska, *Phys. Fluids*, 2010, **22**, 112110.
15 M. Reichert, *Hydrodynamic Interactions in Colloidal and Biological Systems*, PhD thesis, University of Konstanz, 2006.
16 D. Das and D. Saintillan, *Phys. Rev. E: Stat., Nonlinear, Soft Matter Phys.*, 2013, **87**, 043014.
17 A. Varshney, S. Ghosh, S. Bhattacharya and A. Yethiraj, *Sci. Rep.*, 2012, **2**, 738.
18 L. Kramer and W. Pesch, *Annu. Rev. Fluid Mech.*, 1995, **27**, 515–539.
19 J. D. Posner and J. G. Santiago, *J. Fluid Mech.*, 2006, **555**, 1–42.
20 G. R. Wang, F. Yang and W. Zhao, *Lab Chip*, 2014, **14**, 1452–1458.
21 P. Perlekar, L. Biferale, M. Sbragaglia, S. Srivastava and F. Toschi, *Phys. Fluids*, 2012, **24**, 065101.
22 J. O. Hinze, *AIChE J.*, 1955, **1**, 289–295.
23 C. Garrett, M. Li and D. Farmer, *J. Phys. Oceanogr.*, 2000, **30**, 2163–2171.
24 N. Rashidnia, R. Balasubramaniam, J. Kuang, P. Petitjeans and T. Maxworthy, *Int. J. Thermophys.*, 2001, **22**, 547–555.
25 D. Bonn, F. Ingremeau, Y. Amarouchene and H. Kellay, *Phys. Rev. E: Stat., Nonlinear, Soft Matter Phys.*, 2011, **84**, 045301(R).